Numerical Simulations of Various Rotor Designs in Hover and Forward Flight

T. A. Fitzgibbon*, G.N. Barakos† M. A. Woodgate ‡ A. Jimenez - Garcia §
CFD Laboratory, School of Engineering, University of Glasgow, G12 8QQ Glasgow, UK

This paper presents numerical simulations of different rotor designs using high-fidelity CFD methods. Firstly, hover simulation results are presented for the PSP rotor blade. The impact of a transitional turbulence model on the blade performance is examined and good correlation with test data is shown. Transition location predictions are compared with experiment and other computational studies. The PSP rotor is also simulated in forward flight at three thrust coefficients and blade surface pressure on the advancing and retreating blades is compared with wind tunnel data. The predictions were found to follow the data from the pressure transducers, but not the PSP technique. The second part of the paper focuses on the analysis of a more advanced blade planform in hover, the Langley BERP blade [1]. The performance predictions show good agreement with measured integrated loads. Finally, the impact of anhedral is examined for the Langley BERP blade, and yields performance improvements.

Nomenclature

c	=	rotor chord
C_M, C_{M_x}	=	pitching moment coefficient
C_{M_y}	=	rolling moment coefficient
C_P	=	pressure coefficient
C_Q	=	torque coefficient
C_T	=	thrust coefficient
k	=	turbulent kinetic energy
M	=	Mach number
N	=	amplification factor
P	=	pressure
P_∞	=	freestream pressure

*PhD Student, CFD Laboratory, School of Engineering, Email: t.fitzgibbon.1@research.gla.ac.uk
†Professor, MAIAA, MRAeS, CFD Laboratory, School of Engineering, Email: George.Barakos@glasgow.ac.uk
‡Research Associate, CFD Laboratory, School of Engineering, Email: mark.woodgate@glasgow.ac.uk
§FT Technologies Ltd., Email: a.jimenez-garcia.1@research.gla.ac.uk

r	=	local radial position
R	=	rotor radius
$\mathbf{R}$	=	flow equation residual vector
$Re_{\theta t}$	=	transition momentum thickness Reynolds number
V	=	velocity
$\mathbf{V}$	=	flow equation cell volume
$\mathbf{W}$	=	flow equation solution vector
y	=	chordwise location
y^+	=	dimensionless wall distance
β	=	coning angle
β_{1s}, β_{1c}	=	flapping harmonics
ϵ	=	turbulent dissipation rate
γ	=	turbulent intermittency factor
γ	=	specific heat ratio
ω	=	k-specific turbulent dissipation rate
Ω	=	rotational speed
ψ	=	azimuthal angle
ρ_∞	=	freestream density
σ	=	rotor solidity
θ_s	=	shaft angle
θ_{75}, θ_0	=	collective angle
θ_{1s}, θ_{1c}	=	first pitching harmonics
μ	=	advance ratio
ABS	=	Advancing Blade Side
$AIAA$	=	American Institute of Aeronautics and Astronautics
ALE	=	Arbitrary Lagrangian Eulerian
$BERP$	=	British Experimental Rotor Programme
$BILU$	=	Block Incomplete Lower-Upper
CFD	=	Computational Fluid Dynamics
FoM	=	Figure of Merit
HMB	=	Helicopter Multi-Block
$MUSCL$	=	Monotone Upstream Scheme for Conservations Laws

$NASA$	=	North American Space Administration
$NFAC$	=	National Full-Scale Aerodynamics Complex
PSP	=	Pressure Sensitive Paint
$ROBIN$	=	Rotor Body Interaction
RBS	=	Retreating Blade Side
RTC	=	Rotor Test Cell
SST	=	Shear Stress Transport
TM	=	Turbulence Model
$URANS$	=	Unsteady Reynolds Averaged Navier-Stokes
p	=	due to pressure
ref	=	reference
v	=	due to viscosity
i, j, k	=	cell index
$*$	=	sonic

Introduction

The need for accurate CFD predictions for high performance helicopter rotor design has been recognised for a number of years. In the past, the majority of novel rotor concepts were investigated via wind tunnel and flight tests. A wide range of different planforms have been examined within these studies. This led to different rotor designs to be favoured across the globe. For example, the BERP planform used nearly solely in the UK, whereas other regions of the world tend to use more simpler designs such as a swept/swept-tapered or a parabolic tips as discussed by Brocklehurst and Barakos [2]. The emergence of more radical rotor designs such as the Blue-Edge blade [3] or the new Chinook rotor blade [4], further highlight this point. These differences show that the exact planform shape of an optimum rotor is still unknown. The development of CFD methods and rapid growth in computational power, means that an optimum rotor is likely to emerge through numerical simulation. However, the ability to predict the rotor performance for advanced planforms of modern CFD methods has to be assessed. To do this, there is a growing need for high-quality validation data.

Considerable efforts have been performed within the rotorcraft research community that continue to bridge the gap between CFD and real-life rotor performance. In hover, a wide range of studies were performed within the AIAA Hover Prediction Workshop formed in 2014 [5]. The aim of the workshop was to predict the hover performance of a rotor blade within 0.1 counts in figure of merit. The S-76 model scale rotor experiments performed by Balch [6] were used as the main test case. Code comparisons were made between the project partners using various solvers with different

orders of accuracy, meshing techniques, and turbulence models. The effect of tip shape on the performance of the rotor was also investigated. This workshop showed the need for more in-depth validation data, as only integrated blade loads could be compared with experiment. However, surface pressure predictions, blade loads and wake geometry were compared between the workshop participants but showed differences depending on the modelling approach [7]. This workshop highlighted the issues with current hover simulations such as the wake breakdown and the need for transitional turbulence models for accurate performance predictions. The need for including aeroelastic effects as well as facility/installation effects were also noted.

The PSP rotor has also become an important test case due to available surface pressure data and planned further tests. This rotor was first tested by Wong et al. [8],[9] in the Rotor Test Cell (RTC) of the 14- by 22-ft Subsonic Tunnel, at the NASA Langley Research Center. Although one of the main objectives was to investigate the use of Pressure Sensitive Paint for experimental rotor testing, the results are also important for CFD validation purposes. The surface pressure measurements using transducers and pressure sensitive paint are reported for a range of thrust coefficients in both hover and forward flight [9]. Further tests were performed by Overmeyer and Martin [10] in the same facility, who investigated hover performance and boundary layer transition effects. Future tests of the PSP rotor (with a modified root geometry) are planned in the National Full-Scale Aerodynamics Complex (NFAC) 80- by 120-Foot Wind Tunnel at the NASA Ames Research Center. A higher blade tip Mach number (0.65 compared to 0.58) is planned.

More radical blade designs such as the BERP planform have not yet been the subject of many scientific papers. The BERP planform is known to have superior performance compared to other blade designs at high speed forward-flight and high blade loading, while hover performance compared to for example, a planform with a parabolic blade tip is similar. Since the development of this rotor [11] and with the exception of some works [12],[13],[14] not much validation has been performed for BERP blades. Optimisation of BERP-like tip geometries were performed by Johnson and Barakos [15], but the final shape was not tested in a wind tunnel. To date, the only experimental data concerning BERP-like blades was performed at NASA by Yeager et al. [1]. Integrated loads are reported in hover and forward flight. There is no experimental data regarding the surface pressure distributions, sectional loads and wake geometry for this type of blade.

In this work, hover performance predictions are obtained for the PSP blade as well as the Langley BERP blade. The first part of the paper focuses on the PSP blade. The performance of this blade in hover with the fully-turbulent boundary layer assumption was presented by Jimenez-Garcia and Barakos [16]. In this paper, we examine the effect of a transitional turbulence model on hover performance. The transition locations at each blade loading are compared with experimental data [10] and other computational studies. Further forward flight cases are also examined. The second part of the paper evaluates a more advanced planform in hover, the Langley BERP blade. The performance predictions are compared with experimental data from Yeager et al. [1]. The effect of anhedral on the performance of the Langley BERP blade is studied.

Numerical method

HMB Solver

The Helicopter Multi-Block (HMB) [17, 18] code is used as the CFD solver for the present work. It solves the Unsteady Reynolds Averaged Navier-Stokes (URANS) equations in integral form using the Arbitrary Lagrangian Eulerian (ALE) formulation for time-dependent domains, which may include moving boundaries. The Navier-Stokes equations are discretised using a cell-centred finite volume approach on a multi-block grid. The spatial discretisation of these equations leads to a set of ordinary differential equations in time,

$$\frac{d}{dt}(\boldsymbol{W}_{i,j,k}\ V_{i,j,k}) = -\boldsymbol{R}_{i,j,k}(\boldsymbol{W}) \tag{1}$$

where i, j, k represent the cell index, $\boldsymbol{W}$ and $\boldsymbol{R}$ are the vector of conservative flow variables and flux residual respectively, and $V_{i,j,k}$ is the volume of the cell i, j, k. To evaluate the convective fluxes, the Osher[19] approximate Riemann solver is used, while the viscous terms are discretised using a second order central differencing spatial discretisation. The Monotone Upstream-centred Schemes for Conservation Laws, which is referred to in the literature as the MUSCL approach and developed by Leer [20], is used to provide high-order accuracy in space. The HMB solver uses the alternative form of the Albada limiter [21] being activated in regions where a large gradients are encountered mainly due to shock waves, avoiding the non-physical spurious oscillations. An implicit dual-time stepping method is employed to performed the temporal integration, where the solution is marching in pseudo-time iterations to achieve fast convergence, which is solved using a first-order backward difference. The linearised system of equations is solved using the Generalised Conjugate Gradient method with a Block Incomplete Lower-Upper (BILU) factorisation as a pre-conditioner [22]. To allow an easy sharing of the calculation load for parallel job, a multi-block structured meshes are used.

Turbulence models

Various turbulence models are available in HMB solver, including several one-equation, two-equation, three-equation, and four-equation turbulence models. Furthermore, Large-Eddy Simulation (LES), Detached-Eddy Simulation (DES) and Delay-Detached-Eddy Simulation (DDES) are also available. For this study, the fully-turbulent the k-ω SST model from Menter [23] and transitional k-ω SST-γ [24] turbulence models are employed. Both these models are based on the RANS approach, where the Reynolds stresses are modelled through a linear turbulent eddy viscosity term. Two additional transport equations are employed for the turbulent variables, k and ω, which represent the turbulent kinetic energy and the k-specific dissipation rate. The k-ω SST [23] employs the Wilcox k-ω baseline turbulence

model in the near-wall region (sub-layer and logarithmic region of the boundary layer), and the k-ϵ model is used away from the wall. A blending function is used to combine the two formulations . The full mathematical formulation for the k-ω SST turbulence model can be found in [23]. The k-ω SST-γ model solves an additional transport equation for the turbulent intermittency factor, γ. This model is based on the local correlation-based transition modelling concept. The equation for the transition momentum thickness Reynolds number $Re_{\theta t}$ is avoided, through algebraic computation of the transition onset terms based on the flow Reynolds number. The full formulation of this model can be found in [24]. The model used here, is calibrated for low-Mach number flows as in [25], however, has proven to give good predictions here.

Overset Grid Method

Overset grids and sliding plane methods are available in HMB [18, 26] to allow for the relative motion between different mesh components. Both methods have been employed for isolated rotor blades, such as the UH-60A by Dehaeze *et al.* [27], the S-76 by Jimenez-Garcia *et al.* [28], the XV-15 by Gates [29] and even for complete helicopter configurations [18]. For the present work, an overset grid method is employed to ease the generation of each individual mesh component for hover computations, and to allow for the relative motion between mesh components in forward flight cases.

The overset grid method, also referred to as the chimera method, is based on structured composite grids with hexahedral elements, consisting of independently generated, overlapping non-matching sub-domains. A hierarchical approach is employed allowing to interpolate the solution variables based on an user-specified hierarchy of sub-domains. The interpolation between composite grids depends on a localisation procedure, that includes a localisation pre-processing and a chimera search which aim is to minimise the number of searches due to potential mesh overlap. Three methods are available to control the interpolation needed for the chimera solution; zero order single-neighbour, inverse distance, and variable-distribution reconstruction-based interpolation. Further information about the implementation of the overset grid method in HMB can be found in [26].

Geometry and Computational setup

PSP Rotor Geometry

The four-bladed PSP rotor has an aspect ratio (R/c) of 12.2 and a nominal twist of -14 degrees. The main characteristics of the rotor blades are summarised in Table 1. The blade planform has been generated using three radial stations. First, the RC(4)-12 aerofoil was used up to 65% R. Then, the RC(4)-10 aerofoil from 70% R to 80% R. Finally, the RC(6)-08 aerofoil was used from 85% R to the tip. The aerodynamic characteristics of these aerofoils can be found in [30, 31]. The planform of the PSP model rotor has a 60% tapered and 30° swept tip and the details on the blade radial twist and the chord distributions are shown in Figure 1.

Table 1 Geometric properties of the PSP rotor [32].

Parameter	Value
Number of blades (N_b)	4
Rotor radius (R)	66.50 inches
Rotor blade chord (c)	5.45 inches
Aspect ratio (R/c)	12.2
Rotor solidity (σ)	0.1033
Linear twist angle (Θ)	-14°

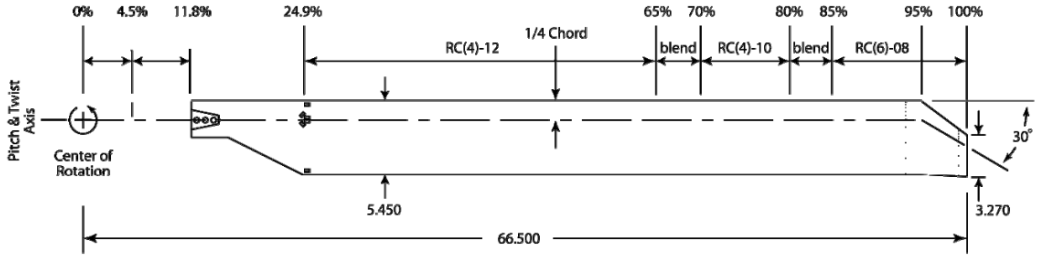

Fig. 1 Planform of the PSP model rotor with a 60% taper and 30° swept tip [33].

Langley BERP Rotor Geometry

The Langley BERP blade was tested at model scale by Yeager et al. [1] at a tip Mach number of 0.628 using a high-density, Freon-12 medium. The Freon-12 gas is used for better matching the test Mach and Reynolds numbers with full-scale values [1]. This rotor as an aspect ratio (R/c) of 13.76 and a geometric solidity of 0.096. The blade uses an RC(4)-10 aerofoil section inboards of the tip section whereas an RC(3)-07 section is used across the blade tip. The outboard section coordinates are not reported in the literature, however an RC(3)-08 section leads to an increase in rotor blade thickness near the BERP-like tip, hence the thickness of aerofoil was scaled. The aerodynamics of these two aerofoils are described by Noonan [30],[31]. The aerofoil transition occurs between 0.84R and 0.866R, which is the notch region of the blade tip. The planform is shown in figure 2

In terms of geometry, there are a few unknowns. The exact shape of the paddle-type tip is scanned from figure 2. The thickness distribution across the tip is also assumed. The RC(3)-07 aerofoil is used up to 0.96%R and then the thickness is tapered off linearly to a assumed trailing edge thickness of 0.04%c. The twist distribution of the Langley BERP blade is shown in figure 3. This blade has a linear twist of approximately 9 degrees. The difference in the zero lift angle between the two aerofoil sections is accounted for in the aerofoil blending region. Finally, no twist is used across the paddle-type tip.

An additional geometry is generated for the Langley BERP blade with 15 degrees parabolic anhedral. The anhedral is initiated from the 0.9545%R station and is shown in figure 4.

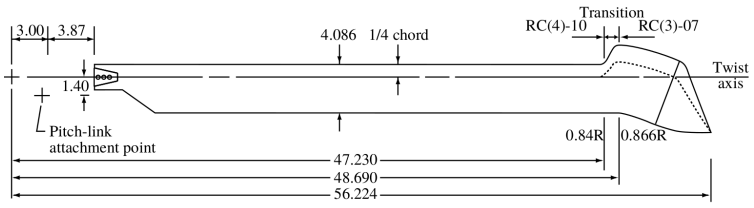

Fig. 2 Blade planform of the Langley BERP rotor [1]

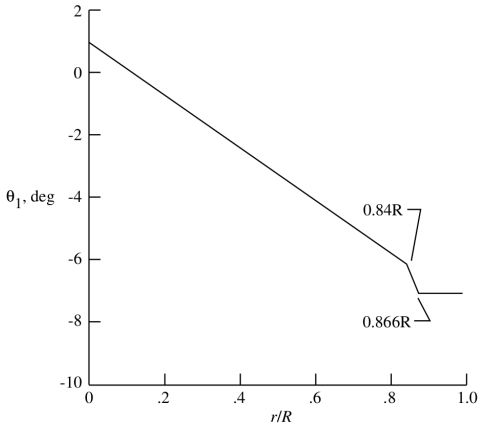

Fig. 3 Twist distribution of the Langley BERP blade [1].

Fig. 4 Geometry of the Langley BERP blade with 15 deg parabolic anhedral, viewed in the streamwise direction.

Computational setup and Meshes for PSP and Langley BERP blades

The chimera technique is used for evaluations of the PSP and Langley BERP blades in hover. Only a quarter of the computational domain was meshed, assuming periodic conditions for the flow field in the azimuthal direction. This assumption is valid if the wake generated by the rotor is assumed periodic and the blades do not experience deep stall. A source/sink model is used for the simulations as shown in figure 5 with a Froude boundary condition imposed at the inflow and outflow. For the blades, a C-topology around the leading edge of the blade was selected, whereas an H-topology was employed at the trailing edge [34]. For the Langley BERP blade, an O-grid is used round the tip of the blade. The topologies of the meshes for both blades are shown in figure 6. Two foreground grids were used for the PSP blade in hover with a transitional turbulence model. The effect of a finer boundary layer was examined, with a reduced near-wall spacing and near-wall expansion ratio. The meshing parameters for the PSP and Langley BERP rotor blades are shown in Table 2.

Table 2 Meshing parameters for the PSP and Langley BERP rotor meshes.

	PSP - Mesh I (hover)	PSP - Mesh II (hover)	Langley BERP - Mesh I (hover)
Background mesh size (cells)	7.2 million	7.2 million	4.9 million
Blade mesh size (cells)	5.2 million	8.1 million	4.6 million
Overall mesh size (cells)	12.4 million	15.3 million	9.5 million
Wall distance	$1.0 \cdot 10^{-5} c_{\text{ref}}$	$1.0 \cdot 10^{-6} c_{\text{ref}}$	$1.0 \cdot 10^{-5} c_{\text{ref}}$
Points along the span	215	215	164
Points around the aerofoil	252	252	222
Points normal to the blade	56	101	66

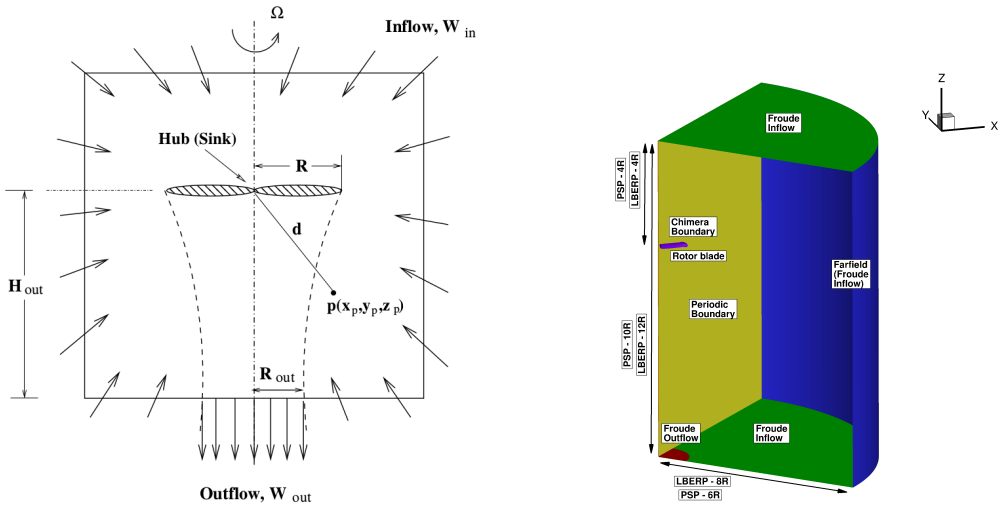

(a) Source - sink model adopted from [35]. (b) Computational domain.

Fig. 5 Source-sink model used for hover simulations (left) and computational domain with employed boundary conditions (right).

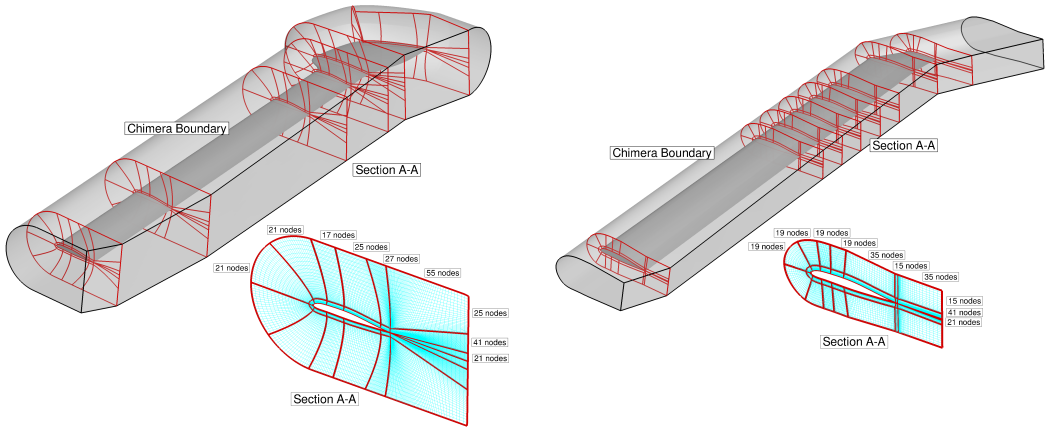

(a) Langley BERP blocking (b) PSP blade blocking

Fig. 6 Blade mesh topologies for Langley BERP (left) and PSP (right) rotor blades.

The PSP rotor was also simulated in forward flight. For these cases the full domain was simulated as the flow is unsteady. The multi-block structured grid used for the PSP rotor in forward flight has a total of 31.6 million cells with 1968 blocks, with 20 and 11.6 million cells for the background and body-fitted grids, respectively. A hub was also included in the computational domain and modelled as a generic ellipsoidal surface.

Simulated Cases

In hover, the PSP blade was simulated using two turbulence models - the fully turbulent k-ω SST model and the transitional k-ω SST-γ models. As a means to validate the pressure sensitive paint (PSP) technique for rotor blades in hover, Wong *et al.* [33] measured C_P at two radial stations and blade-tip Mach number of 0.585 on the PSP rotor blades, which were installed on the modified ROtor BOdy Interaction fuselage (ROBIN Mod7). Recently, Overmeyer *et al.* [36] measured integrated blade loads for free and fixed transition conditions, and transition locations using the same conditions in the same facility (Rotor Test Cell at the NASA Langley Research Center 14×22 Foot Subsonic Wind Tunnel). His tests are simulated here in out-of-ground effect (OGE) conditions, for fully-turbulent and transitional boundary layer assumptions. The transitional cases are simulated using two grids, to study the effect of a finer near-wall spacing. The free-stream turbulence values for the transitional simulations correspond to a critical N-factor of 9 and eddy viscosity ratio of 1. The Reynolds number, based on the reference blade chord c_{ref} of 5.45 inches and on the blade-tip speed, was $1.94 \cdot 10^6$.

The PSP rotor is also simulated in high-speed forward flight at three thrust coefficients. Additionally to the previously presented case at medium loading of $C_T = 0.006$ [16], cases at $C_T = 0.004$ and $C_T = 0.008$ are also shown here. The data obtained from these simulations is compared with experimental data from Wong et al. [9]. The tests were performed at an advance ratio of $\mu = 0.35$, and the freestream Mach number was 0.2, giving a free-stream Reynolds number of 6.98×10^5. To meet the target thrust coefficients for each case, whilst having zero roll and pitching moments, a matrix trimming method is used in HMB [17], based on the Blade Element Theory (BET) for computing the elements of the sensitivity matrix. The flow solutions were computed solving the URANS equations, coupled with Menter's k-ω SST turbulence model [23]. The employed time step corresponds to 0.25 deg in the azimuthal direction and was based on experience gained with previous rotor computations in forward flight [18].

The Langley BERP blade was simulated in hover at four collectives at a tip Mach number of 0.628. The integrated loads were compared with experimental data from Yeager et al. [1]. The experimental data was performed in Freon-12 which has a higher density than air, allowing tests close to full scale Reynolds numbers. The hover experiments were performed in minor ground effect of z/d=0.83, however the ground is not modelled in these simulations. The Reynolds number was calculated based on Freon density of 3.09227 kg/m^3 and dynamic viscosity of $12.357 \times 10^{-6} Pa/s$. The reference velocity was calculated based on the rotational tip Mach number of 0.628 and speed of sound equal to 153.924 m/s (giving a value of $V_{ref} = 95.664 m/s$). The reference length used was the chord of the first aerodynamic section.

This gives a Reynolds number based on the tip speed equal to 2.51×10^6. A specific heat ratio of 1.128 (compared to 1.4 for air) was also used within the CFD simulations. An additional case was ran to assess the effect of anhedral in hover for the Langley BERP geometry.

Table 3 summarises the employed conditions and the computations performed in hover. The values of blade pitch and coning angles alongside thrust coefficient and turbulence model (TM in Table 3) employed are also reported. The computed forward flight cases are presented in table 4.

Table 3 Computational cases for the PSP rotor and Langley BERP rotors in hover. TM=Turbulence model; SST=Shear Stress Transport [23].

Blade	**Mesh**	M_{TIP}	θ_{75}**(deg)**	β**(deg)**	C_T	**TM**
PSP	Mesh I	0.585	4°	0°	0.00259	$k-\omega$ SST
PSP	Mesh I	0.585	6.58°	1.39°	0.00503	$k-\omega$ SST
PSP	Mesh I	0.585	8.48°	2.44°	0.00694	$k-\omega$ SST
PSP	Mesh I	0.585	9.46°	3.02°	0.00797	$k-\omega$ SST
PSP	Mesh I	0.585	10.3°	3.5°	0.00893	$k-\omega$ SST
PSP	Mesh I	0.585	12°	0°	0.01059	$k-\omega$ SST
PSP	Mesh I	0.585	6.57°	1.39°	0.00500	$k-\omega$ SST-γ
PSP	Mesh II	0.585	6.52°	1.34°	0.00499	$k-\omega$ SST-γ
PSP	Mesh I	0.585	8.43°	2.40°	0.00708	$k-\omega$ SST-γ
PSP	Mesh II	0.585	8.40°	2.37°	0.00698	$k-\omega$ SST-γ
PSP	Mesh I	0.585	10.18°	3.40°	0.00919	$k-\omega$ SST-γ
PSP	Mesh II	0.585	10.16°	3.37°	0.00903	$k-\omega$ SST-γ
LBERP	Mesh I	0.628	9°	0°	0.00720	$k-\omega$ SST
LBERP	Mesh I	0.628	10.5°	0°	0.00883	$k-\omega$ SST
LBERP	Mesh I	0.628	12°	0°	0.01045	$k-\omega$ SST
LBERP	Mesh I	0.628	13.5°	0°	0.01211	$k-\omega$ SST
LBERP (15 deg anhedral)	Mesh I	0.628	10.5°	0°	0.00888	$k-\omega$ SST

Table 4 Computational cases for the PSP rotor in forward flight. TM=Turbulence model; SST=Shear Stress Transport [23].

Blade	μ	$\mathbf{M}_{\text{inf}}$	C_T	**TM**
PSP	0.35	0.2	0.004	$k-\omega$ SST
PSP	0.35	0.2	0.006	$k-\omega$ SST
PSP	0.35	0.2	0.008	$k-\omega$ SST

Results and Discussion

PSP rotor in hover

Integrated blade loads

Figure 7 shows the variation of FoM and torque coefficient with the blade loading coefficient, at six blade pitch angles, covering low, medium, and high thrust (see Table 3) for both fully-turbulent and transitional boundary layer predictions. Comparison with experimental data (black circles) by Overmeyer *et al.* [36] for the fixed-transition, 5% c, upper and lower (run 156) and transition free (run 118) are included. Two sets of published CFD simulations are also included for direct comparison, including transitional effects. Vieira *et al.* [37] employed the commercial software Star-CCM+ (orange diamond symbols) with the Spalart-Almaras turbulence model and the Spalart-Almaras - e^N model for transition predictions. Green triangle symbols correspond to numerical simulations performed by Rohit [38] with the structured OVERFLOW solver, for an isolated rotor (without fuselage) (see Rohit [38], Figure 10). The $k-\omega$ SST and $k-\omega$ SST γ-Reθ turbulence models were used in this work. Note that the experiments reported here does not correspond to the isolated PSP rotor, thus some degree of discrepancy on the airloads is expected.

At low thrust $C_T/\sigma < 0.06$, it can be seen that all CFD computations are in close agreement with experiments. Good correlation is seen for the fully-turbulent boundary layer cases, whereas the transitional predictions are slightly overpredicted. As at these thrust levels, a high contribution of profile drag exists, the predictions of the transitional locations will have a large impact on the performance prediction. Such thrust levels, are not however, attributable to any real-life scenario as for many helicopters, this loading is under the empty weight of the vehicle. At medium thrust levels the predictions agree very well with experimental data for both fully-turbulent and transitional cases. The results between the three computational studies, are also in very good agreement. At high thrust, the scatter is larger. The data of Vieira [37] overpredicts the performance, whereas the data of HMB3 leads to an underpredicted figure of merit. Rohit ([38], Figure 10) evaluated the effect of rotor installation on the FoM, and it was found that the installed-rotor FoM presents a higher values (around 1.4 counts of FoM) when compared with the isolated rotor at $C_T/\sigma \approx 0.094$, which perhaps is one of the sources of discrepancy, at high thrust, between HMB3 and experiments. The transitional cases, however, show better agreement with experiment. The finer mesh is the wall normal direction improves the predictions at all thrust levels, leading to a reduced performance at low loading and increased figure of merit at high thrust levels. The PSP rotor is also found to have a high performance sensitivity due to transition effects, as the performance is improved by 7.5 counts in figure of merit at low thrust and 5 counts at higher thrust levels. Such large performance benefits would not be expected on full-scale helicopters in flight, due to higher atmospheric turbulence, vibration and surface roughness/erosion. However, for correlation with wind tunnel test data, transitional effects are seen to be significant.

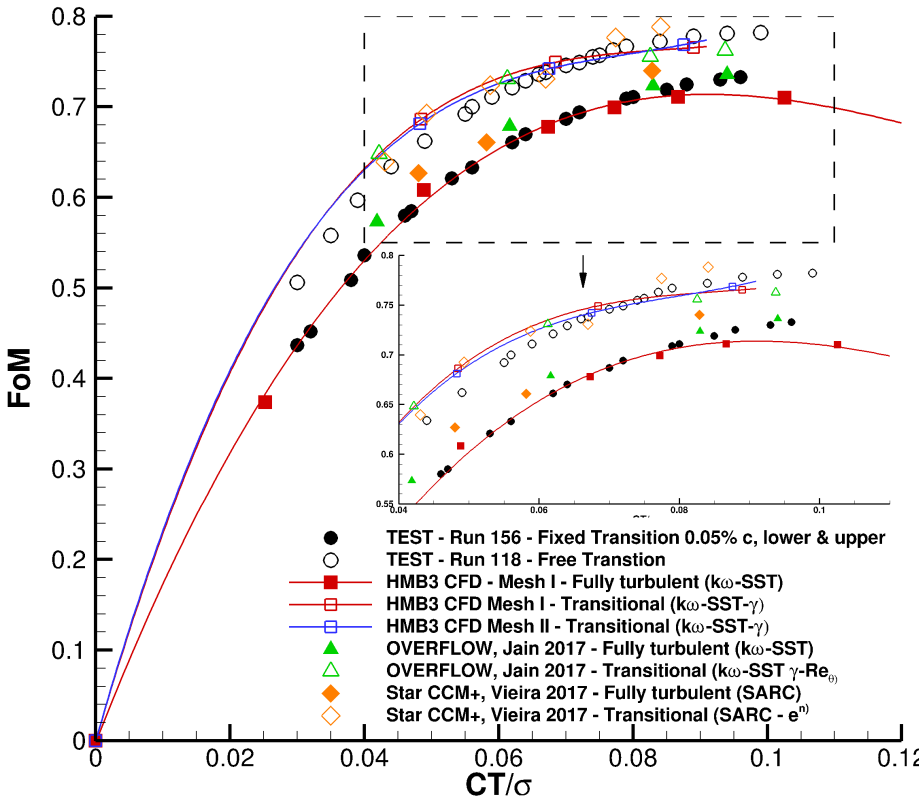

Fig. 7 C_T/σ**-FoM for the PSP model rotor at blade-tip Mach number of 0.585 in hover using the fully-turbulent boundary layer and transitional flow assumptions. Comparisons with published CFD data: OVERFLOW [38], Star CCM+ [37] and experimental data [36] are also shown.**

Surface pressure predictions

Surface pressure coefficients (C_P) are compared between CFD and experimental data [9, 33] at two radial stations (r/R= 0.93 and 0.99) on the upper surface of the PSP blade on the Mesh I (see Table 2) and using the fully-turbulent k-ω SST model. The C_P is computed based on the local velocity at each radial station:

$$C_P = \frac{P - P_\infty}{1/2\rho_\infty(\Omega r)^2}. \tag{2}$$

Regarding the experiments, two techniques were used to measured C_P distributions, the Kulite pressure transducers (square symbols) and the PSP technique (dashed lines) in Figures 8-9. A reasonable agreement is seen by both techniques for both stations at the four thrust coefficients considered here; C_T= 0.005, 0.007, 0.008, and 0.009. CFD results are able to predict the overall distribution of C_P at both stations, and the pressure at the trailing edge is also well captured. It is noticeable that discrepancies appear to be present, when sections at higher thrust are analysed. In fact, the CFD predictions reveal a slightly over-predicted C_P, even if the pressure at the trailing edge is well captured.

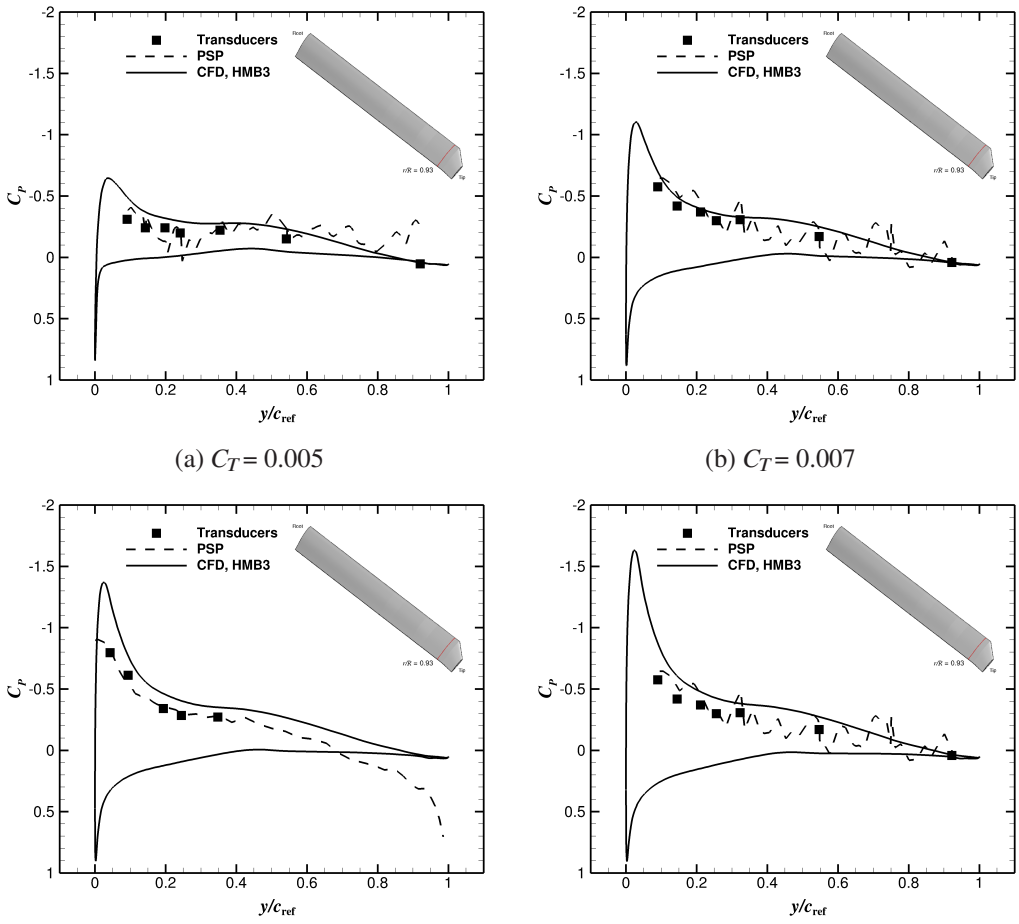

(a) C_T= 0.005 (b) C_T= 0.007

(c) C_T= 0.008 (d) C_T= 0.009

Fig. 8 C_P profile comparisons between experimental data using the PSP technique (dashed line) and pressure tap (square symbols) [9, 33] and CFD (solid line) at radial station $r/R = 0.93$.

Transitional results - grid sensitivity

Grid refinement in the wall-normal direction is examined in more detail for the transitional cases at three thrust coefficients of $C_T = 0.005$,0.007 and 0.009. The baseline PSP mesh, used for fully-turbulent calculations, was refined, to improve the resolution of the boundary layer for transitional predictions. A y^+ of 1 near the wall is, however, obtained in both employed grids. The integrated loads, predictions including the viscous and pressure terms, are shown for both grids in table 5.

Based on table 5, it can be stated, that at lower loading, increasing the number of points in the boundary layer, increases the profile drag contribution leading to closer correlation with experimental data. At higher thrust, the viscous and pressure terms of the torque have a similar contribution for both grids. The improved comparison with experimental data, comes from both a reduced net thrust and torque leading to a slightly higher figure of merit. These differences are mainly due to different predictions in the transition locations at low blade loading at two radial stations.

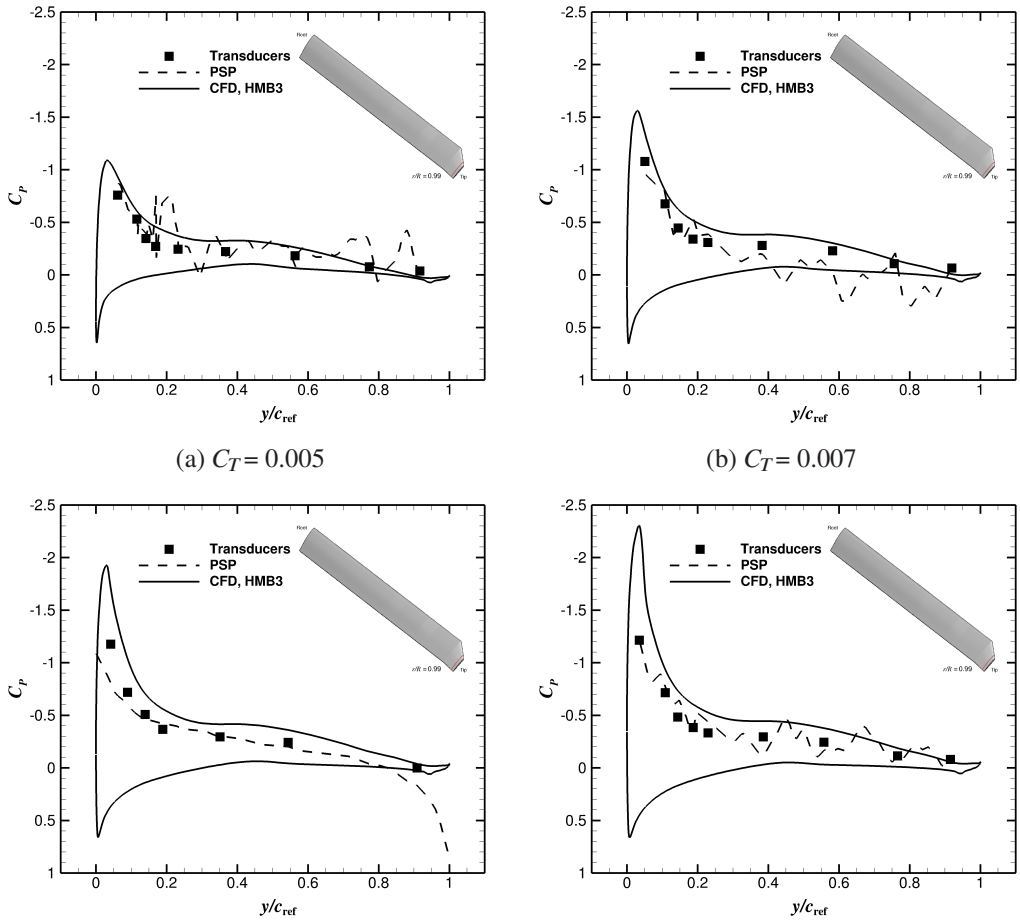

(a) C_T= 0.005 (b) C_T= 0.007

(c) C_T= 0.008 (d) C_T= 0.009

Fig. 9 C_P **profile comparisons between experimental data using the PSP technique (dashed line) and pressure tap (square symbols) [9, 33] and CFD (solid line) at radial station** $r/R = 0.99$**.**

Table 5 Effect of wall-normal spacing on the hover performance of the PSP blade using the k-ω **SST-**γ **turbulence model**

Case	C_{Q_p} in %	C_{Q_v} in %	FoM	FoM error
C_T = 0.005 (EXP)	-	-	0.662	-
C_T = 0.005 (Mesh I)	82.45%	17.55%	0.686	+2.4 counts
C_T = 0.005 (Mesh II)	82.07%	17.93%	0.681	+1.9 counts
C_T = 0.007 (EXP)	-	-	0.738	-
C_T = 0.007 (Mesh I)	89.21%	10.79%	0.749	+0.9 counts
C_T = 0.007 (Mesh II)	88.87%	11.13%	0.742	+0.4 counts
C_T = 0.009 (EXP)	-	-	0.778	-
C_T = 0.009 (Mesh I)	91.80%	8.20%	0.765	-1.3 counts
C_T = 0.009 (Mesh II)	91.85%	8.15%	0.769	-0.9 counts

At low thrust, the bottom surface of the rotor blade, remains laminar for a larger portion of the chord for the grid with coarser wall normal spacing as shown in figure 10. This leads to a reduction in the viscous torque term. With increasing thrust the section where differences can be seen in the transition locations moves further outboards.

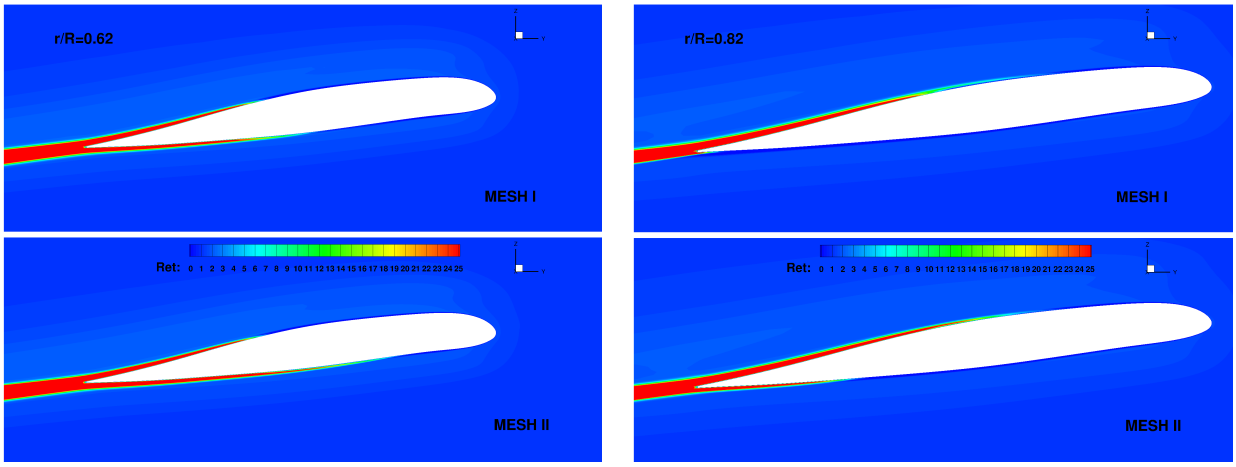

(a) C_T= 0.005, r/R =0.62 (b) C_T= 0.007, r/R =0.82

Fig. 10 Eddy viscosity ratio contours at two thrust coefficients showing differences in the transition locations between the two grids employed.

Transition location predictions

An indicative result for the transition location predictions along the blade span is presented for the case at C_T/σ = 0.048. The results for the grid with finer wall spacing are presented in figure 11. The predictions from HMB3 are compared with experimental data of Overmeyer and Martin [36] and results from Star CCM+ [37].

Figure 11 shows good agreement for the transition location compared with experimental data. On the upper surface, the transition location moves downstream, further inboards (r/R= 0.68) compared to the test data (r/R=0.84). A similar observation can be made for the Star CCM+ results, however this location is further outboards (r/R=0.78) compared to HMB3 predictions. The upper surface predictions across the blade tip are similar for both computational studies and show good correlation with experimental data. On the lower surface, the HMB3 prediction show excellent agreement with experiment. The Star CCM+ predictions, show two regions of early transition along the blade span, not captured by HMB3 results or experiment. Both CFD results predict a laminar flow across the blade tip, whereas the experimental data measured transition before the trailing edge of the blade. The neglection of cross flow instabilities in the transitional turbulence model may introduce errors in the transition location predictions. Further sources of error include turbulence model calibration and freestream turbulence values, which were not reported by experiment.

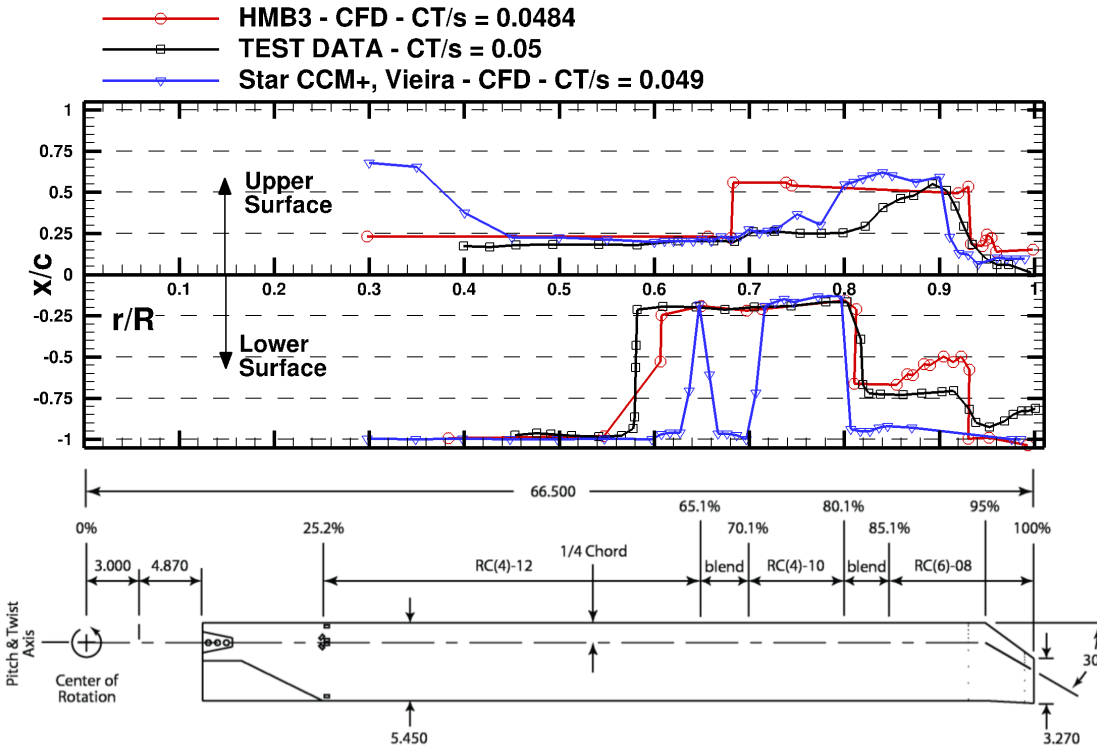

Fig. 11 Predicted transition locations at C_T/σ=0.0484 and comparison with test data [36] and Star CCM+ predictions [37].

Effect of transition on blade loads

The effect of transition is examined further by comparing the sectional blade loads for the fully-turbulent and transitional cases. The sectional thrust and torque distributions are shown in figure 12. The pressure and viscous contributions to the total torque are also shown. The loads are scaled by blade tip velocity and reference blade chord (equal to the chord of the first aerodynamic section).

The overall torque is reduced, when accounting for flow transition as expected. This is especially visible in the region where the preceding blade tip vortex interacts with the blade at r/R = 0.85-0.9, which is mainly due to the pressure torque term as seen from figure 12 c). The viscous torque contributions is also reduced, especially in inboard locations and across the blade tip, as transition location predictions indicated a laminar lower surface of the tip for all examined thrust coefficients. The thrust coefficient distributions do not vary as much as the sectional torque. Slight differences can be seen inboards, where slightly higher thrust is seen for the transitional cases. The peak in the thrust also changes with transition, with a minor increase in thrust at higher loading, and reduction at low loading. The effect of transition on the blade loading is examined further by comparing the chordwise pressure distributions at four radial stations of r/R = 0.75, 0.85, 0.95 and 0.975, which are presented in figure 13.

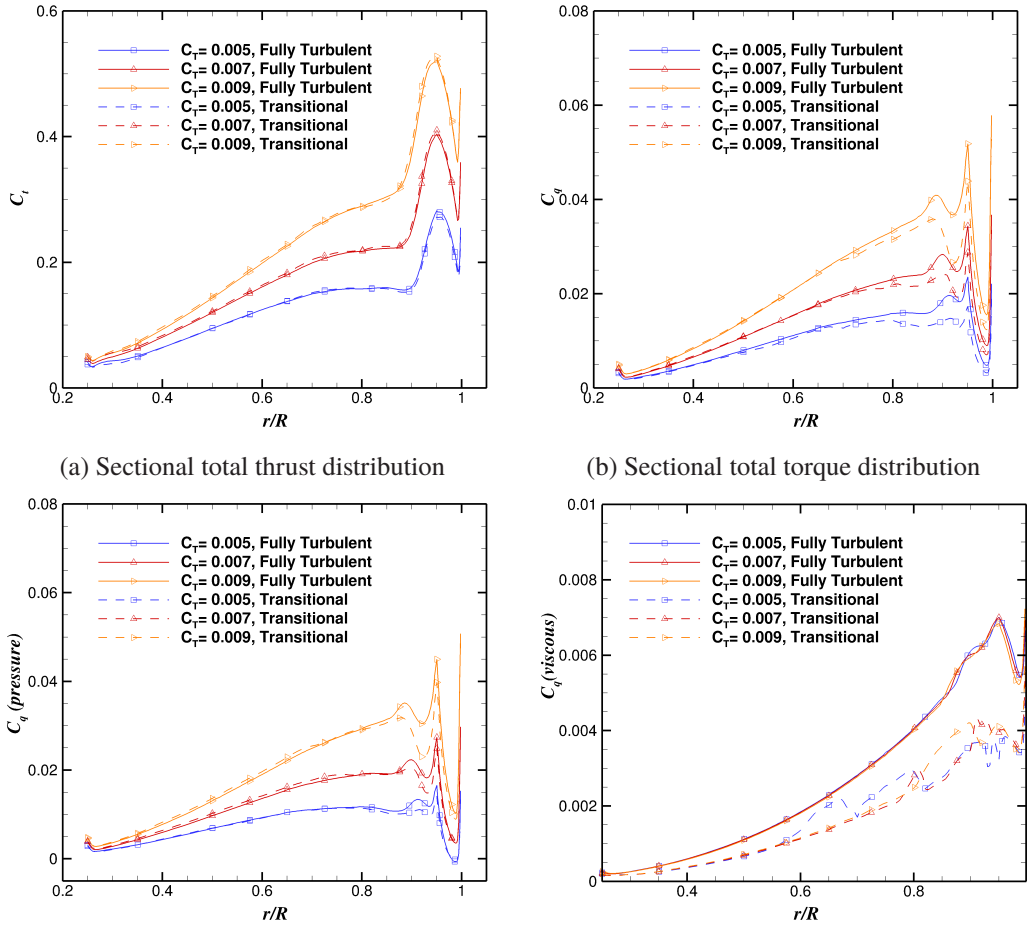

(a) Sectional total thrust distribution

(b) Sectional total torque distribution

(c) Sectional pressure torque distribution

(d) Sectional viscous torque distribution

Fig. 12 Effect of transition on the sectional thrust and torque distributions for the PSP rotor blade in hover and three thrust coefficients.

The changes in the surface pressure due to transition are subtle. The transition location, can clearly be identified on the surface pressure graphs, especially on the upper surface at higher loading, where an abrupt change in the adverse pressure gradient is seen. These features are highlighted in figure 13, by black circles. Changes in the magnitude of the suction peak are mainly noticeable at the highest thrust coefficient, especially in figure 13 (b). This is in agreement with the sectional loads, where the reduction in suction leads to a reduction in torque due to pressure, at this location. The effect of transition on the surface pressure is not very large, and thus the torque due to pressure does not change as much as the viscous torque term, which approach as much as 40%, as shown in figure 12 (d). This is due to a significantly reduced overall skin friction for the transitional cases. The skin friction contour plots for the upper surface at two thrust coefficients are shown in figure 14.

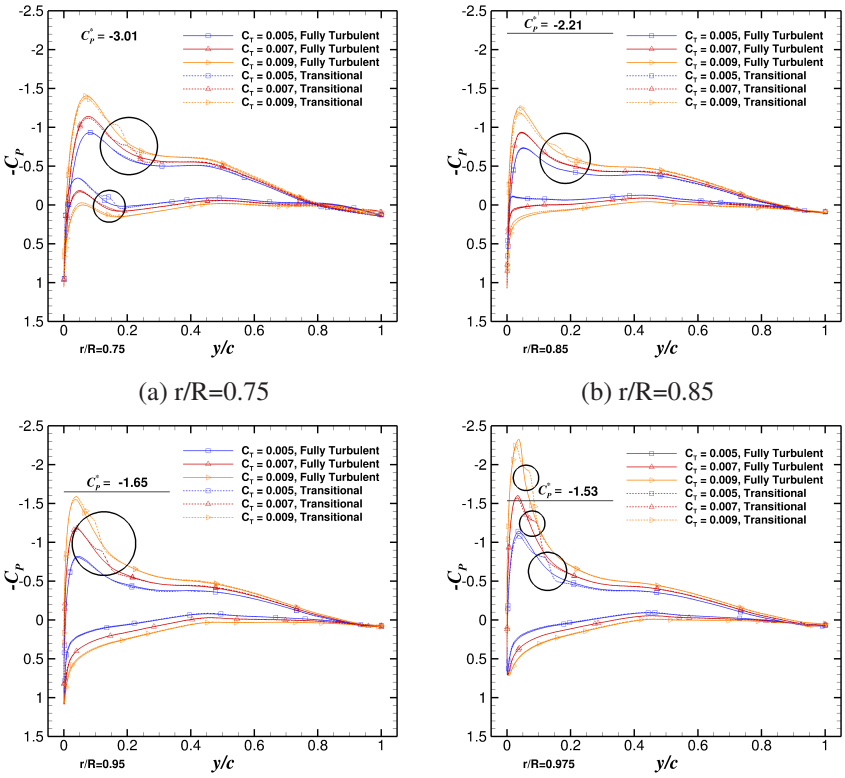

(a) r/R=0.75 (b) r/R=0.85

(c) r/R=0.95 (d) r/R=0.975

Fig. 13 Effect of transition on the chordwise surface pressure coefficient at four radial stations for three thrust coefficients

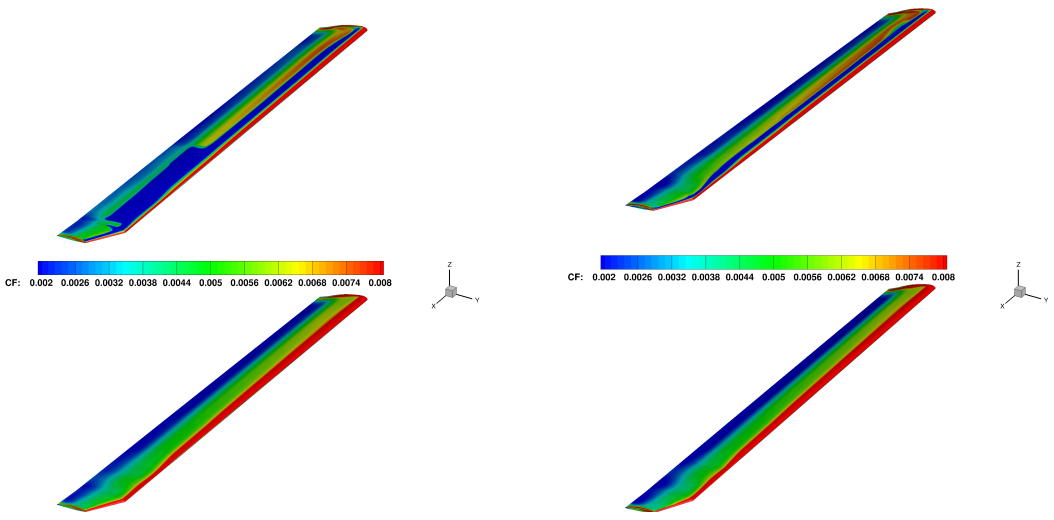

(a) C_T = 0.005 (b) C_T = 0.009

Fig. 14 Effect of transition on the surface skin friction coefficient at low and high thrust, fully-turbulent boundary layer (bottom) and transitional case (top)

PSP blade in Forward Flight

The PSP main rotor was also simulated at medium-speed forward flight. The rotor advance ratio was μ= 0.35, the freestream Mach number 0.2 and the blade tip Mach number equal to 0.58. Experimental data for the surface pressure predictions was obtained by Wong et al. [9] at four thrust conditions. Here, we present the forward flight predictions at C_T = 0.004, C_T = 0.006 and C_T = 0.008. The trim states are specified in Table 6. Note that the negative Fourier series is used with the HMB solver. Note that the negative Fourier series is used with the HMB solver.

Table 6 Trim states for the PSP rotor in forward flight at three thrust levels.

Required C_T	0.004	0.006	0.008
Trimmed C_T	0.00406	0.00600	0.00804
C_{M_x}	3.574×10^{-5}	1.265×10^{-6}	2.660×10^{-5}
C_{M_y}	4.049×10^{-5}	9.642×10^{-7}	9.498×10^{-6}
θ_s	6.0	6.0	6.0
θ_0	6.117	8.324	10.560
θ_{1s}	4.536	6.840	8.956
θ_{1c}	-2.558	-3.392	-4.732
β_0	2.206	3.280	3.346
β_{1s}	-0.501	-0.643	-1.171
β_{1c}	-0.252	-0.780	-0.917

The disk loads for the three cases are presented in figures 15. The normal force indicates a thrust loss region on the advancing side for all three cases, which reduces with increasing thrust coefficient. As the thrust coefficient goes up, the front and back of the disk start to produce a higher normal force. The reverse flow region can also be seen by a negative normal force in the inboard region of the retreating side. The torque coefficient distributions show regions of high torque at the back of the disk. With increasing thrust, higher torque is also observed on the retreating side and front of the rotor disk. On the advancing blade, regions of negative torque were observed when only the pressure term was accounted for. In this region the skin friction has a large contribution to the total torque. The moment distribution does not vary greatly with thrust coefficient. A slightly higher nose-up (positive) moment can be seen on the retreating side and back of the disk at higher thrust coefficients.

Like for the PSP blade in hover, at a blade-tip Mach number of 0.585, experimental surface pressure coefficient are available at the station r/R=0.99 at the ABS and RBS of the rotor the three simulated thrust coefficients. Two techniques were used to measured C_P distributions, the Kulite pressure transducers (square symbols) and the non-intrusive PSP technique (dashed lines) in Figure 16. CFD results were extracted at the ABS (ψ = 100°) and RBS (ψ = 260°), while experimental C_P were measured at 101° and 262°. Note that the PSP data is sample at the 98.2%R station. Regarding the ABS side, a large discrepancy is seen by both techniques. CFD results are able to predict the overall distribution of C_P and follow the Kulite C_P data quite well. The same behaviour is found at the retreating side where CFD predictions

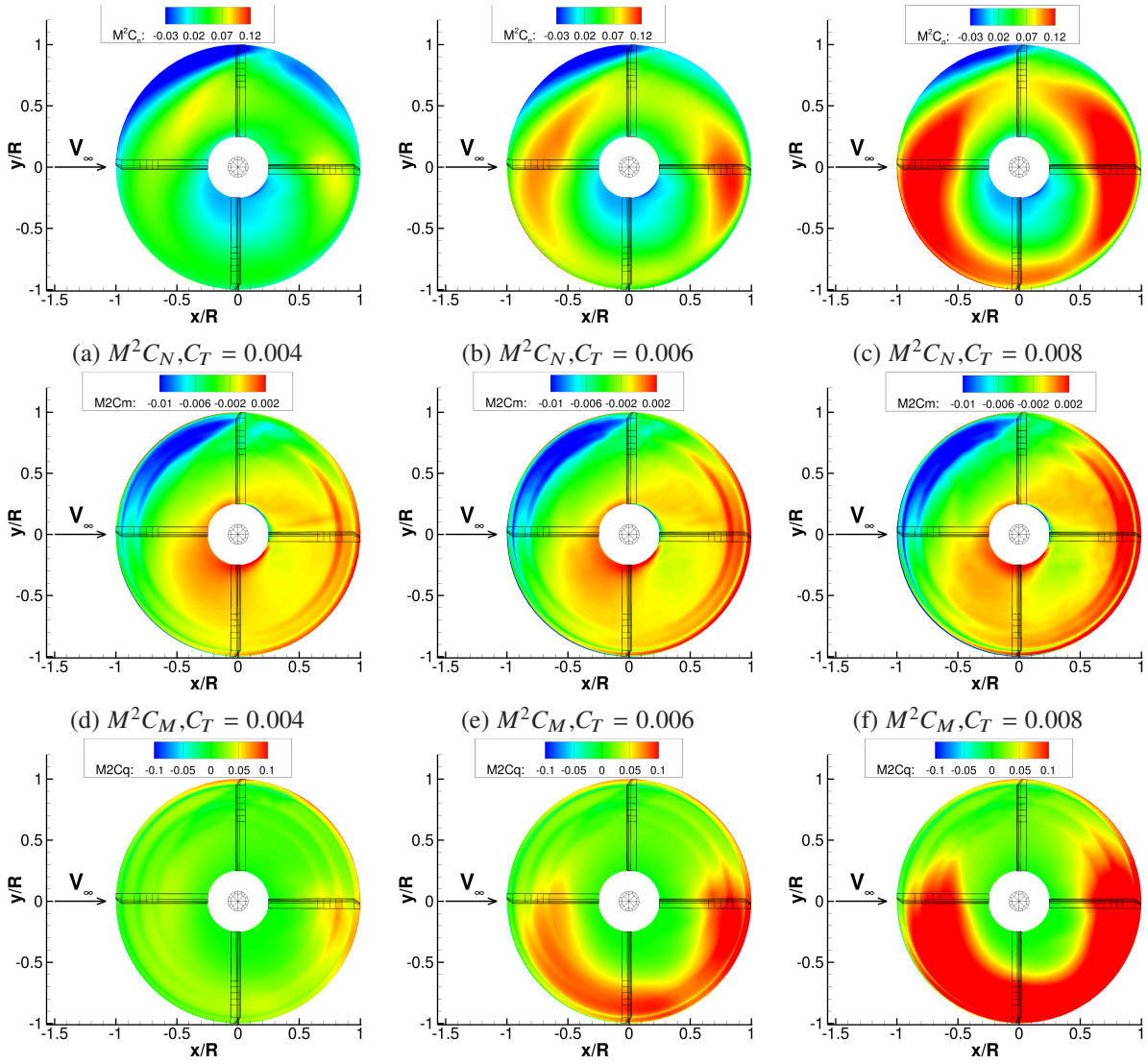

(a) M^2C_N,C_T = 0.004 (b) M^2C_N,C_T = 0.006 (c) M^2C_N,C_T = 0.008

(d) M^2C_M,C_T = 0.004 (e) M^2C_M,C_T = 0.006 (f) M^2C_M,C_T = 0.008

(g) M^2C_Q,C_T = 0.004 (h) M^2C_Q,C_T = 0.006 (i) M^2C_Q,C_T = 0.008

Fig. 15 Predicted rotor disk loads for the PSP rotor in forward flight at advance ratio μ=0.35 at three thrust coefficients.

are in close agreement with the Kulite data too.

Finally, the PSP rotor flowfield is visualized using the Q-criterion at two thrust coefficients of C_T = 0.004 and C_T = 0.008 and is presented in Figure 17. The main wake structures are well resolved for each of the cases. For both cases, the wake is fastly convected downstream due to the high advance ratio. For the high thrust case, a higher downwash is produced by the rotor, hence the wake is convected further downwards in the axial direction compared to the low thrust case. The wake structures away from the rotor are better resolved for the high thrust case, as higher number of mesh points are used in the vicinity of the rotor. As both cases were performed at the same advance ratio, the flow structures are fairly similar.

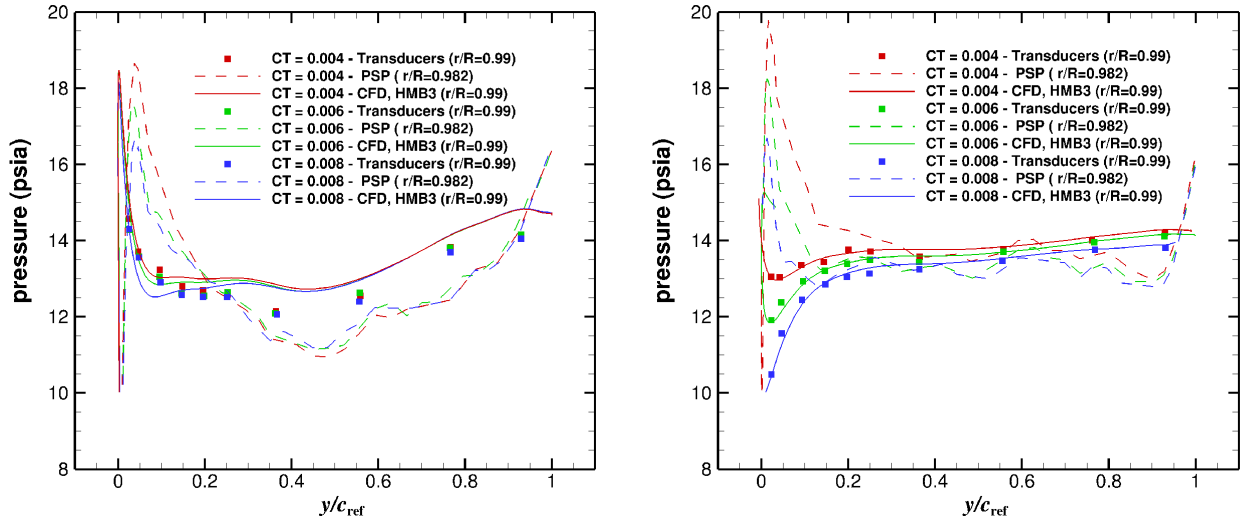

(a) Advancing blade side

(b) Retreating blade side

Fig. 16 Surface pressure predictions for the PSP blade in forward flight at three thrust levels. Comparisons are shown for the advancing and retreating blade sides with experimental data from transducers and the PSP technique [9]

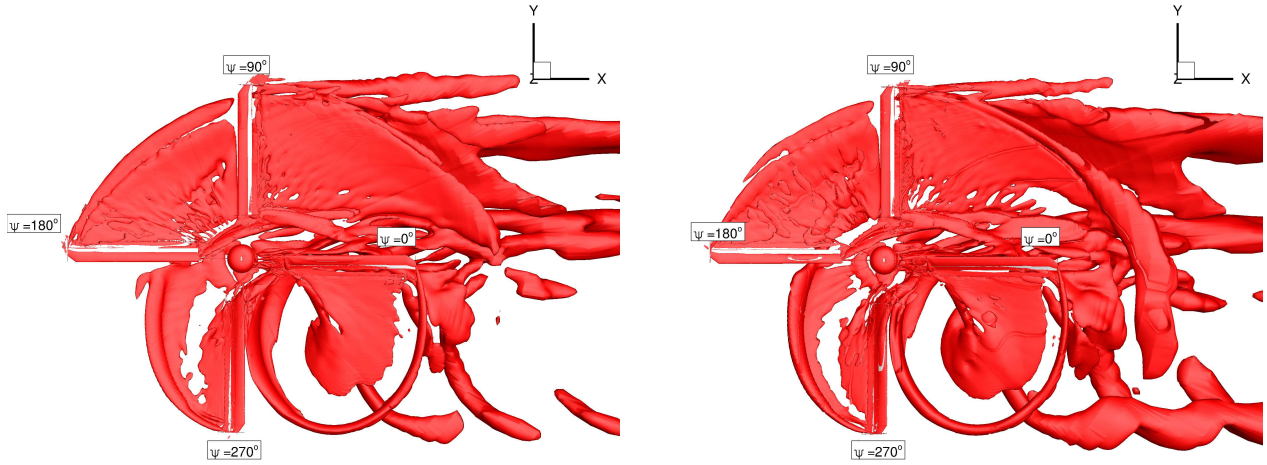

(a) C_T = 0.004

(b) C_T = 0.008

Fig. 17 Wake visualisation for the low and high thrust cases using Q-criterion (value of 0.002) showing similar wake geometries for the PSP rotor in forward flight at μ=0.35.

Langley BERP blade in hover

Integrated blade loads

Figure 18 presents the performance of the Langley BERP blade in hover. The data obtained from CFD simulations is compared with experimental data from Yeager et al. [1].

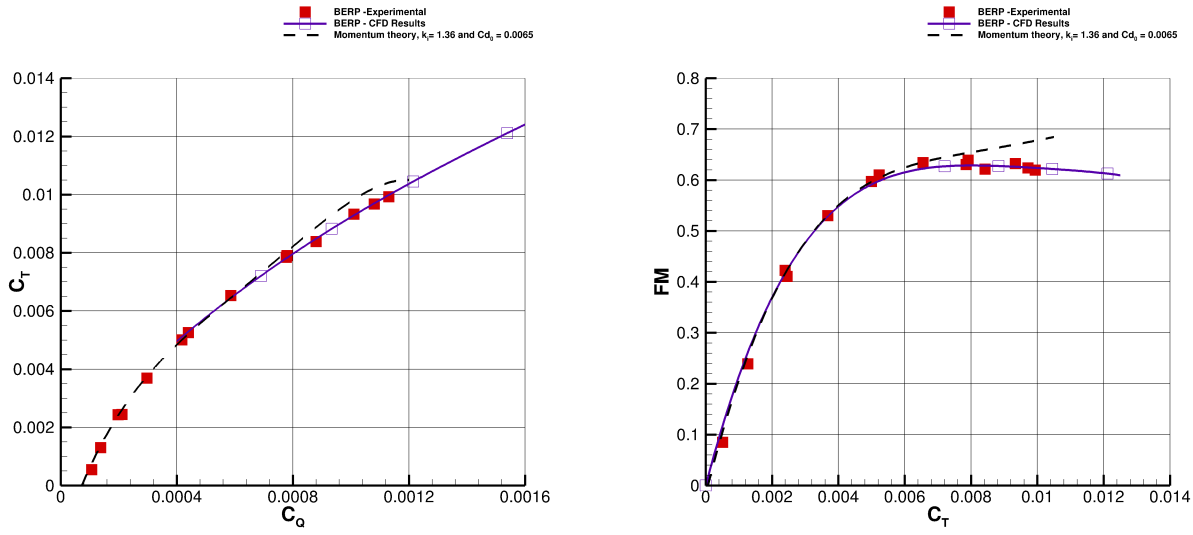

(a) C_Q vs C_T (b) FoM vs C_T

Fig. 18 Integrated loads for the Langley BERP blade in hover and comparison with experimental data for Yeager et al. [1].

The hover performance predictions show very good agreement with experimental data. Despite, neglecting the minor ground effect of the tests, the numerical simulations are able to predict the performance of the Langley BERP blade. A slight scatter can be observed in the experimental data, however, the curves from computation fit well within the experimental test points. The trends of each curves are captured well, with the Langley BERP blade figure of merit curve flattening out at higher thrust coefficients as predicted by experiment. The high thrust case does not see a severe loss in performance as would be seen on other blades such as a rectangular blade. This is in agreement with literature [12],[11] and highlights good performance of the BERP blade at high loading. The performance of the Langley BERP blade is examined further by looking at sectional loads and surface pressure distributions.

Sectional loads

The sectional thrust and torque coefficients for the Langley BERP are shown in figure 19. Both coefficients are normalised with the local flow velocity at each radial station and the reference blade chord equal to the chord of the first aerodynamic section.

The Langley BERP blade continues to deliver a similar increase in thrust with each increase in collective. The effect of the blade geometry is also visible in the thrust and torque sectional distributions. Across the BERP-like tip the

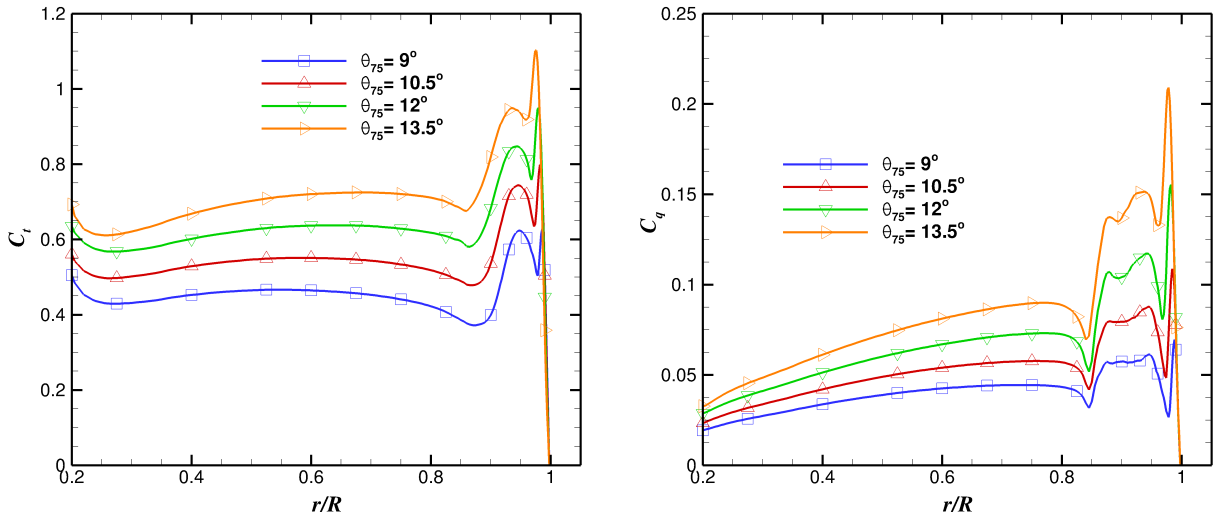

(a) Sectional C_T distribution

(b) Sectional C_Q distribution

Fig. 19 Sectional thrust and torque coefficient distributions for the Langley BERP blade in hover at four collectives.

local thrust is increased due to a larger local chord, which can be seen in the region of r/R=0.9-0.95. The effect of the notch is clear from the sectional torque distributions, where a reduction in local torque is observed at approximately 0.85 r/R. A higher torque is seen across the blade tip compared to more conventional designs due to high outboard planform area.

Surface pressure predictions

The blade surface pressure predictions are shown for the Langley BERP blade at four radial stations in figure 20. The surface pressures coefficients are extracted based on the local velocity at each station. The critical C_P using equation 3 is also calculated and shown, to asses the regions of the blade where the flow becomes supersonic.

$$C_P^* = \frac{2}{\gamma(M_{\text{tip}}\frac{r}{R})^2}\left[\left(\frac{2+(\gamma-1)(M_{\text{tip}}\frac{r}{R})^2}{\gamma+1}\right)^{\frac{\gamma}{\gamma-1}} - 1\right] \tag{3}$$

A strong adverse pressure gradient can be seen at the r/R=0.95 station as the pressure recovers from the leading edge suction peak. Further outboards, however, the adverse pressure gradient is weaker and the pressure recovery is of milder fashion. This is especially visible at higher collective. The main reasoning for this behaviour of the pressure gradient at this station is the formation of the tip vortex inboards of this station for the BERP blade. For this type of geometry, the tip vortex forms and rolls up around the curved blade tip, further inboards compared to for example, a rectangular planform, for which this process occurs at the very tip of the blade.

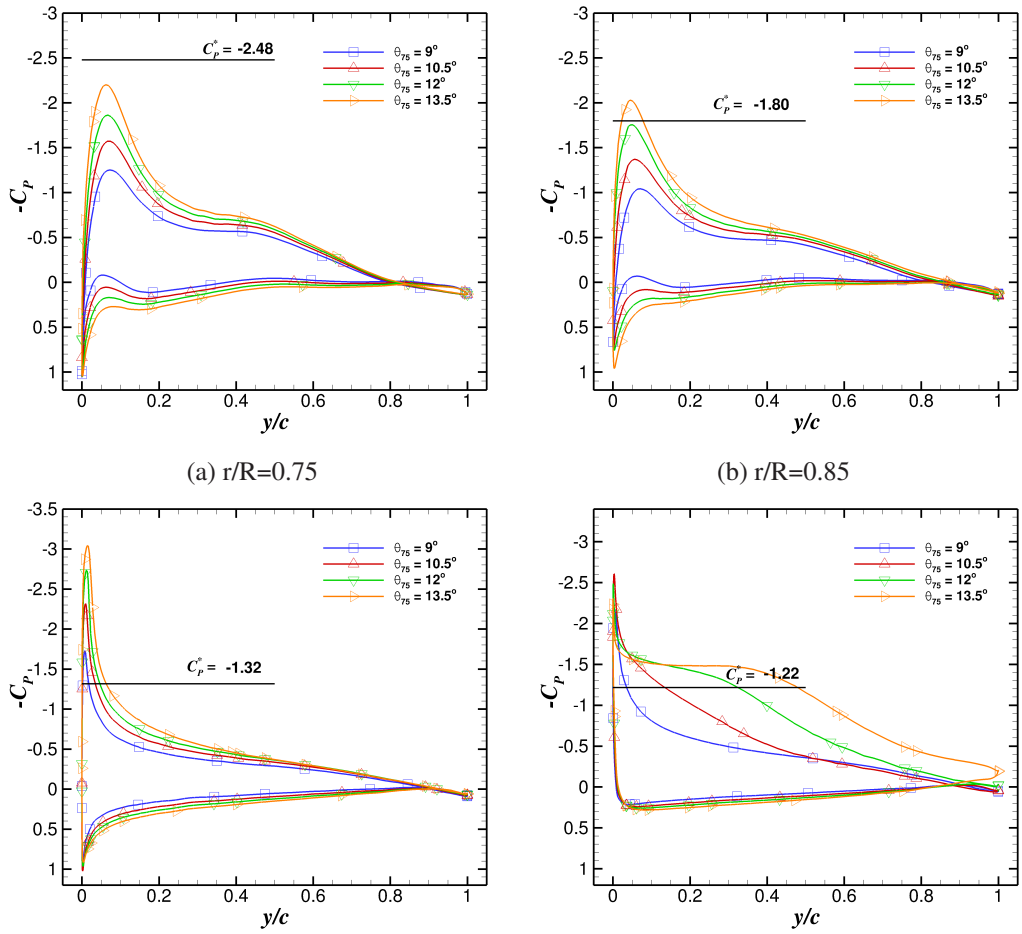

(a) r/R=0.75 (b) r/R=0.85

(c) r/R=0.95 (d) r/R=0.975

Fig. 20 Surface pressure coefficient predictions at four radial stations for the Langley BERP blade in hover.

Wake visualisation

Finally, the wake structures must be extracted from the solution, to ensure that the tip vortices are well resolved. This is shown in figure 21 using an isosurface of Q-criterion coloured with downwash velocity.

The wake visualisation plots shown the the tip vortices up until the 4th passage are well captured by the simulated mesh. This is enough to get good performance predictions as was shown by the integrated loads results. For even better wake resolution, a higher order scheme can be used, or a finer background mesh, however, this will not have a large effect on the performance predictions. The tip vortex formation locations confirms the pressure predictions, as can be seen for the wake visualisation, especially for the higher collective. The tip vortex for the Langley BERP blade starts further inboards, close to the end of the sweep section. A clear vortex is also seen at the location of the notch, which was predicted by past studies in literature [12]. This vortex is of opposite rotational sense compared to the tip vortex, and thus induces a nose-up pitching moment that counteracts the strong nose-down pitching moment induced by the tip vortex. Finally, some numerical noise is seen in the wake visualisations due to the Chimera boundary interpolation.

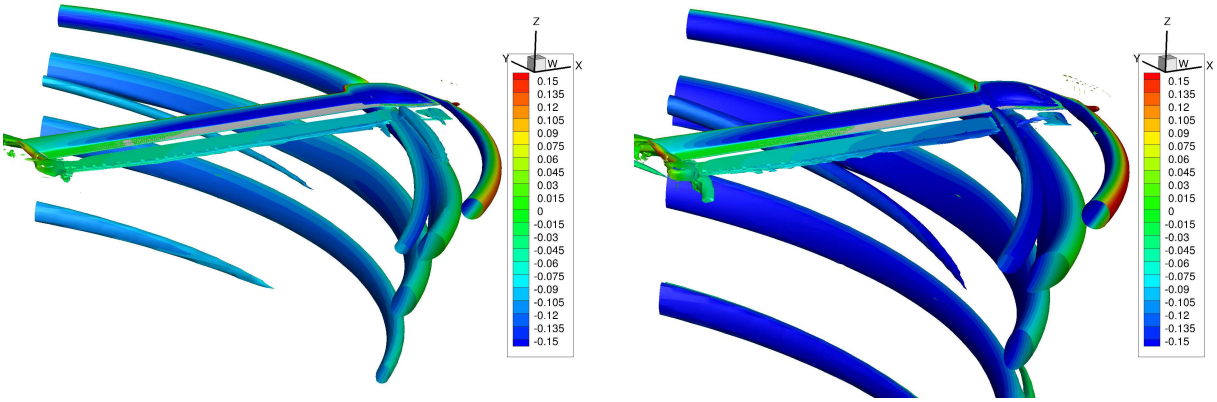

(a) $\theta_{75} = 9^o$ (b) $\theta_{75} = 13.5^o$

Fig. 21 Wake visualisation using an isosurface of Q-criterion (value of 0.005) coloured with downwash velocity for the Langley BERP blade in hover at two collectives.

Langley BERP blade with 15 degrees anhedral

Table 7 Hover performance comparison of standard Langley BERP, and blade with 15 degrees parabolic anhedral.

Blade	C_T	C_Q	FoM	FoM % improvement
LBERP	0.00882	0.000934	0.6276	-
LBERP with 15 deg anhedral	0.00888	0.000883	0.6698	+6.7%

As can be seen from table 7 a 6.7% improvement can be achieved in terms of Figure of Merit for the Langley BERP blade with anhedral. The reasoning behind the better performance is examined further by extracting the sectional loads from the solution. The sectional thrust and torque coefficient distributions are shown in figure 22. The coefficients are normalised by the local flow velocity, hence the differences between the blade with and without anhedral are augmented inboards.

The anhedral produces the same effect as additional negative twist on the radial thrust and torque distributions. The blade tip is offloaded, and a portion of the blade load is moved inboards. This leads to a more optimal induced lift distribution leading to reduced overall torque and hence higher performance. This is further confirmed by examining the surface pressure coefficient distributions shown in figure 23.

Figure 23 indicates that anhedral reduces the suction at the blade tip caused by formation of the tip vortex. The blade tip is offloaded leading to improved aerodynamic performance. A higher blade loading can be also observed inboards, as the suction peak inboards of the notch is slightly increased. The pressure contours bunch up before reaching the tip of the blade. This is perhaps due to a too aggressive reduction in blade thickness at the blade tip.

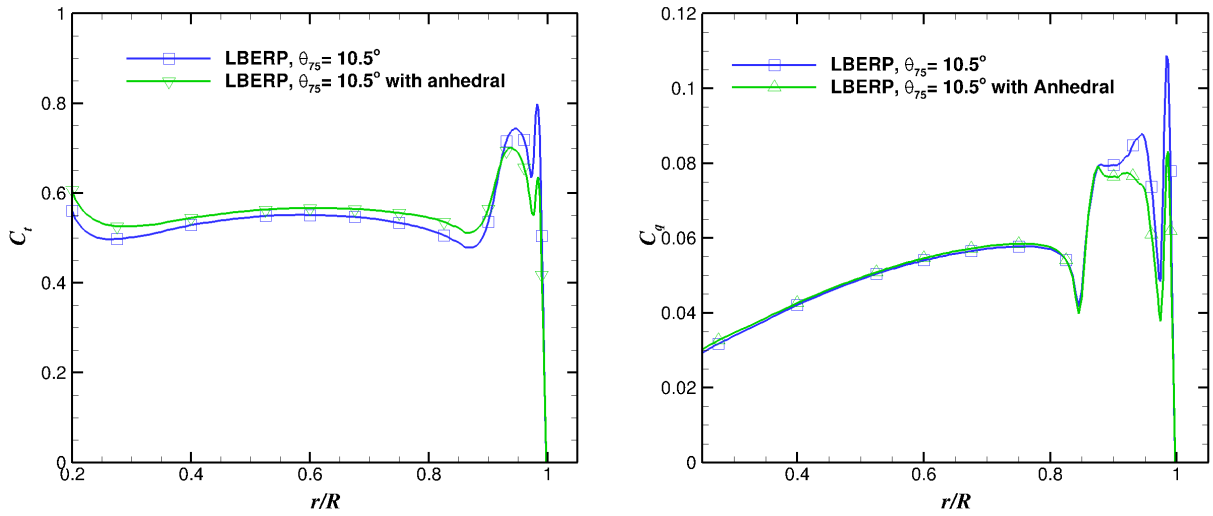

(a) Sectional C_T (b) Sectional C_Q

Fig. 22 Comparison of sectional thrust and torque coefficient distributions for the Langley BERP blade in hover with and without anhedral.

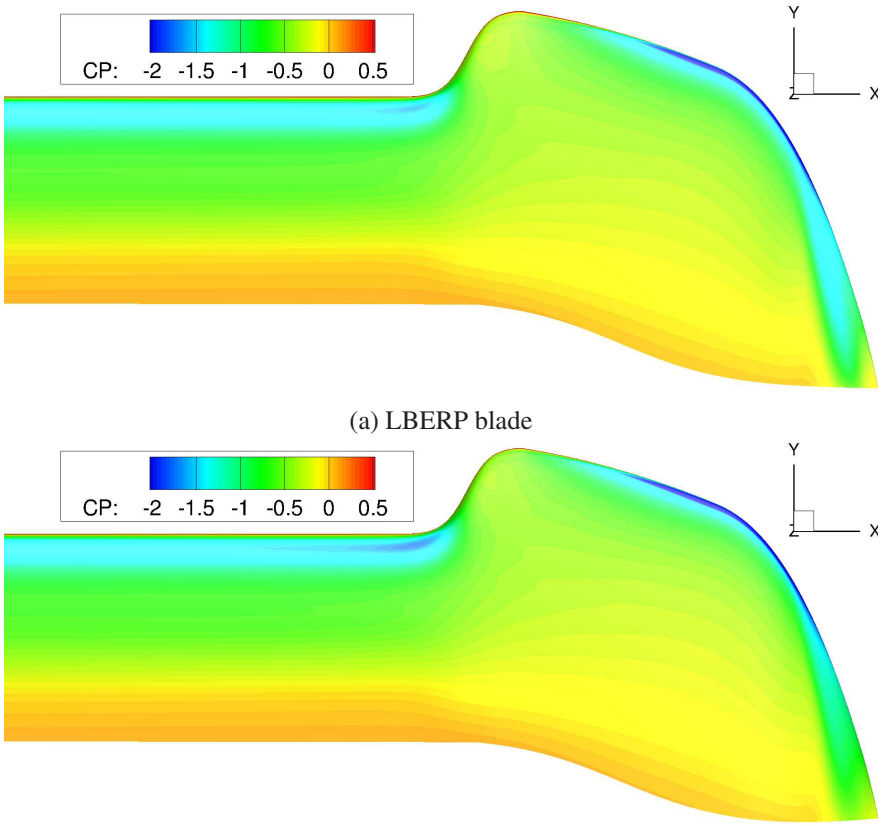

(a) LBERP blade

(b) LBERP blade with 15 deg anhedral

Fig. 23 Comparison of surface pressure distributions (normalised by local flow velocity) for the Langley BERP blade in hover with and without anhedral.

Conclusions

The results for the PSP rotor confirm that modern CFD methods are able to accurately predict the performance of such a blade in hover and forward flight. In hover, very good agreement is obtained with experimental data for the integrated loads for both fully-turbulent and transitional turbulence models. The surface pressure predictions also show good correlation with experiment. The transition locations agree well with the data from Overmeyer et al. [10], with potential improvements needed in the spanwise location where the blade interacts with the preceding blade tip vortex.

In forward flight no integrated loads data is available, however, the surface pressure results are in line with experimental data. In the examined flight conditions, the CFD results agree better with the data obtained with the pressure transducers rather than with the PSP technique. The PSP technique fails to capture the correct trends, especially on the retreating side, where the dynamic pressure is low.

Additionally, the Langley BERP blade was simulated in hover. Based on the very good agreement with experimental data, it can be stated that the CFD method is able to capture the effect of the advanced geometry on the hover performance. First computations, also show that advanced planforms require careful computational optimisation. This is due to the strong sensitivity of geometric features such as anhedral on the blade performance, as shown in this paper.

The numerical simulations within this paper have shown that very good hover and forward flight predictions can be obtained with modest computational resources. A more comprehensive dataset is required for in-depth CFD validation, in order to verify the predictions and flow field physics behind more advanced blade planforms.

Acknowledgements

This work is funded by DSTL (Defence Science and Technology Laboratory). This publication contains information authorized for unlimited release and distribution under the auspices of The Technical Cooperation Program (TTCP). The technical work has been completed under the collaboration project, TTCP AER CP13.A1, Next Generation Rotor Blade Design. Results were obtained using the EPSRC funded ARCHIE-WeSt High Performance Computer (www.archie-west.ac.uk). EPSRC grant no. EP/K000586/1. This work used the Cirrus UK National Tier-2 HPC Service at EPCC (http://www.cirrus.ac.uk)

References

[1] Yeager Jr, W., Noonan, K., Singleton, J., Wilbur, M., and Mirick, P., "Performance and Vibratory Loads Data From a Wind-Tunnel Test of a Model Helicopter Main-Rotor Blade With a Paddle-Type Tip," Tech. rep., National Aeronuatics and Space Administration, 1997. NASA-TM-4754.

[2] Brocklehurst, A., and Barakos, G., "A review of helicopter rotor blade tip shapes," *Progress in Aerospace Sciences*, Vol. 56, 2013, pp. 35 – 74.

[3] Rauch, P., Gervais, M., Cranga, P., Baud, A., Hirsch, J., Walter, A., and Beaumier, P., "Blue Edge (TM): The Design, Development and Testing of a New Blade Concept," *American Helicopter Society 67th Annual Forum*, 2011.

[4] Boeing, "New Chinook Composite Blades Proven," `http://www.boeing.com/features/2017/01/chinook-blades-01-17.page`, 2017. [Online; accessed 22-March-2018].

[5] Hariharan, N., Egolf, T., and Sankar, L., "Simulation of Rotor in Hover: Current State and Challenges," *AIAA SciTech Forum, 52th Aerospace Sciences Meeting*, 2014.

[6] Balch, D., and J.Lombardi, "Experimental Study of Main Rotor Tip Geometry and Tail Rotor Interactions in Hover, Vol I - Text and Figures," Tech. rep., National Aeronautics and Space Administration, 1985. NASA-CR-177336-Vol-1.

[7] Hariharan, N., Narducci, R., Reed, E., and Egolf, T., "Helicopter Aerodynamic Modeling of Rotor with Tip-Shape Variations: AIAA Standardized Hover Evaluations," *AIAA SciTech Forum, 54th Aerospace Sciences Meeting*, 2016.

[8] Wong, O., Watkins, A., and Ingram, J., "Pressure Sensitive Paint Measurements on 15% Scale Rotor Blades in Hover," *35th AIAA Fluid Dynamics Conference and Exhibit*, 2005.

[9] Wong, O., Watkins, A., Goodman, K., Crafton, J., Forlines, A., Goss, L., Gregory, J., and Juliano, T., "Blade Tip Pressure Measurements using Pressure Sensitive Paint," *American Helicopter Society 68th Annual Forum*, 2012.

[10] Overmeyer, A., and Martin, P., "Measured Boundary Layer Transition and Rotor Hover Performance at Model Scale," *AIAA SciTech Forum, 55th AIAA Aerospace Sciences Meeting*, 2017.

[11] Perry, F., "Aerodynamics of the World Speed Record," *43rd Annual Forum of the American Helicopter Society*, 1987.

[12] Scott, M., Sigl, D., and Strawn, R., "Computational and Experimental Evaluation of Helicopter Rotor Tips for High-Speed Flight," *Journal of Aircraft*, Vol. 28, No. 6, 1991, pp. 403–409.

[13] Srinivasan, G., Raghavan, V., and Duque, E., "Flowfield Analysis of Modern Helicopter Rotors in Hover by Navier-Stokes Method," *International Technical Specialists Meeting on Rotorcraft Acoustics and Rotor Fluid Dynamics*, 1991.

[14] Duque, E., "A Numerical Analysis of the British Experimental Rotor Program Blade," *45th Annual Forum of the American Helicopter Society*, 1989.

[15] Johnson, C., and Barakos, G., "Optimizing Rotor Blades with Approximate British Experimental Rotor Programme Tips," *Journal of Aircraft*, Vol. 51, No. 2, 2014.

[16] Jimenez-Garcia, A., and Barakos, G., "Numerical Simulations on the PSP Rotor Using HMB3," *AIAA SciTech Forum, 56th Aerospace Sciences Meeting*, 2018.

[17] Steijl, R., Barakos, G. N., and Badcock, K., "A framework for CFD analysis of helicopter rotors in hover and forward flight," *International Journal for Numerical Methods in Fluids*, Vol. 51, No. 8, 2006, pp. 819–847. DOI: 10.1002/d.1086.

[18] Steijl, R., and Barakos, G. N., "Sliding mesh algorithm for CFD analysis of helicopter rotor-fuselage aerodynamics," *International Journal for Numerical Methods in Fluids*, Vol. 58, No. 5, 2008, pp. 527–549. DOI: 10.1002/d.1757.

[19] Osher, S., and Chakravarthy, S., "Upwind schemes and boundary conditions with applications to Euler equations in general geometries," *Journal of Computational Physics*, Vol. 50, No. 3, 1983, pp. 447–481. DOI: 10.1016/0021-9991(83)90106-7.

[20] van Leer, B., "Towards the ultimate conservative difference scheme. V.A second-order sequel to Godunov's Method," *Journal of Computational Physics*, Vol. 32, No. 1, 1979, pp. 101–136. DOI: 10.1016/0021-9991(79)90145-1.

[21] van Albada, G. D., van Leer, B., and Roberts, W. W., "A Comparative Study of Computational Methods in Cosmic Gas Dynamics," *Astronomy and Astrophysics*, Vol. 108, No. 1, 1982, pp. 76–84.

[22] Axelsson, O., *Iterative Solution Methods*, Cambridge University Press: Cambridge, MA, 1994.

[23] Menter, F. R., "Two-Equation Eddy-Viscosity Turbulence Models for Engineering Applications," *AIAA Journal*, Vol. 32, No. 8, 1994, pp. 1598–1605. DOI: 10.2514/3.12149.

[24] Menter, F. R., Smirnov, P. E., Liu, T., and Avancha, R., "A One-Equation Local Correlation-Based Transition Model," *Flow Turbulence Combust*, Vol. 95, No. 4, 2015, pp. 583–619. DOI:10.1007/s10494-015-9622-4.

[25] Colonia, S., Leble, V., Steijl, R., and Barakos, G., "Assessment and calibration of the /$gamma$ equation transition model for a wide range of Reynolds numbers at low Mach," *AIAA Journal*, Vol. 55, No. 4, 2016, pp. 1126–1139.

[26] Jarkowski, M., Woodgate, M., Barakos, G. N., and Rokicki, J., "Towards consistent hybrid overset mesh methods for rotorcraft CFD," *International Journal for Numerical Methods in Fluids*, Vol. 74, No. 8, 2014, pp. 543–576. DOI: 10.1002/fld.3861.

[27] Dehaeze, F., and Barakos, G. N., "Aeroelastic CFD Computations for Rotor Flows," *Proceedings of the Thirty-Seventh European Rotorcraft Forum*, ERF, Galarate, Italy, 2011, pp. 1–20.

[28] Jimenez, A., and Barakos, G. N., "Hover Predictions on the S-76 Rotor using HMB2," *Proceedings of the Fifty-Third Aerospace Sciences Meeting*, AIAA, Kissimmee, Florida, 2015, pp. 1–34.

[29] Gates, S., "Aerodynamic Analysis of Tiltrotors in Hovering and Propeller Modes Using Advanced Navier-Stokes Computations," *Proceedings of the Thirty-Ninth European Rotorcraft Forum*, ERF, Moscow, Russia, 2013, pp. 1–26.

[30] Noonan, K. W., "Aerodynamic Characteristics of Two Rotorcraft Airfoils Designed for Application to the Inboard Region of a Main Rotor Blade," NASA TP-3009, U.S. Army Aviation Systems Command, TR-90-B-005, Jul. 1990.

[31] Noonan, K. W., "Aerodynamic Characteristics of Two Rotorcraft Airfoils Designed for Application to the Inboard Region of a Main Rotor Blade," NASA TM-4264, U.S. Army Aviation Systems Command, TR-91-B-003, May 1991.

[32] Watkins, A. N., Leighty, B. D., Lipford, W. E., Goodman, K. Z., Crafton, J., and Gregory, J. W., "Measuring Surface Pressures on Rotor Blades Using Pressure-Sensitive Paint," *AIAA Journal*, Vol. 54, No. 1, 2016, pp. 206–215. DOI:http://dx.doi.org/10.2514/1.J054191.

[33] Wong, O. D., Noonan, K. W., Watkins, A. N., Jenkins, L. N., and Yao, C. S., "Non-Intrusive Measurements of a Four-Bladed Rotor in Hover - A First Look," *Proceedings of the American Helicopter Society Aeromechanics Specialists*, AHS-2010, San Francisco, California, 2010, pp. 1–11.

[34] Jimenez-Garcia, A., and Barakos, G. N., "Accurate Predictions of Rotor Hover Performance at Low and High Disc Loadings," *Journal of Aircraft*, Vol. 1, No. 1, 2017, pp. 1–12. DOI: 10.2514/1.C034144.

[35] Srinivasan, G., "A Free-Wake Euler and Navier-Stokes CFD Method and its Application to Helicopter Rotors Including Dynamic Stall," DAAL03-90-C-0013, 1993.

[36] Overmeyer, A. D., and and, P. B. M., "Measured Boundary Layer Transition and Rotor Hover Performance at Model Scale," *Proceedings of the 55th Aerospace Sciences Meeting*, AIAA-2017-1872, Grapevine, Texas, 2017, pp. 1–36.

[37] Vieira, B. A. O., Kinzel, M. P., and Maughmer, M. D., "CFD Hover Predictions Including Boundary-Layer Transition," *Proceedings of the 55th Aerospace Sciences Meeting*, AIAA-2017-1665, Grapevine, Texas, 2017, pp. 1–16.

[38] Rohit, J., "CFD Performance and Turbulence Transition Predictions on an Installed Model-scale Rotor in Hover," *Proceedings of the 55th Aerospace Sciences Meeting*, AIAA-2017-1871, Grapevine, Texas, 2017, pp. 1–29.